





Electronic ground state of two nonmagnetic pentavalent honeycomb iridates

A. de la Torre ¹, B. Zager,¹ J. R. Chamorro,^{2,3} M. H. Upton,⁴ G. Fabbris ⁴, D. Haskel ⁴,
D. Casa,⁴ T. M. McQueen,^{2,3,5} and K. W. Plumb ¹

¹*Department of Physics, Brown University, Providence, Rhode Island 02912, USA*

²*Department of Chemistry, The Johns Hopkins University, Baltimore, Maryland 21218, USA*

³*Institute for Quantum Matter, William H. Miller III Department of Physics and Astronomy, Johns Hopkins University, Baltimore, Maryland 21218, USA*

⁴*Advanced Photon Source, Argonne National Laboratory, Argonne, Illinois 60439, USA*

⁵*Department of Materials Science and Engineering, The Johns Hopkins University, Baltimore, Maryland 21218, USA*



(Received 17 June 2022; accepted 27 July 2022; published 8 August 2022)

We investigate the electronic structure of two Ir^{5+} honeycomb iridates, $\text{Sr}_3\text{CaIr}_2\text{O}_9$ and NaIrO_3 , by means of resonant x-ray techniques. We confirm that $\text{Sr}_3\text{CaIr}_2\text{O}_9$ realizes a large spin-orbit driven nonmagnetic $J_{\text{eff}} = 0$ singlet ground state despite sizable tetragonal distortions of Ir coordinating octahedra. However, the resonant inelastic x-ray spectra of NaIrO_3 are drastically different from expectations for a Mott insulator with octahedrally coordinated Ir^{5+} . We find that the data for NaIrO_3 can be best interpreted as originating from a narrow gap nonmagnetic $S = 0$ band insulating ground state. Our results highlight the complex role of the ligand environment in the electronic structure of honeycomb iridates and the essential role of x-ray spectroscopy to characterize electronic ground states of insulating materials.

DOI: [10.1103/PhysRevMaterials.6.084406](https://doi.org/10.1103/PhysRevMaterials.6.084406)

I. INTRODUCTION

New emergent correlated phenomena have been predicted to arise in materials with $4/5d$ transition metals in where spin-orbit coupling (λ) and electron-electron correlations (U) are the dominant energy scales, including topologically protected magnetic states and complex magnetic orders. The essential physics occurs at the single ion level. Operating within the j - j coupling limit, the interplay of cubic crystal field and spin orbit coupling acts to generate a quartet with pseudospin $j_{\text{eff}} = 3/2$ and a $j_{\text{eff}} = 1/2$ doublet states from the d electron levels [1]. Depending on the electron filling, the j_{eff} states form the basis for many novel quantum phases including Kitaev spin liquids [2], spin-orbital liquids [3–5], multipolar phases [3], and other unconventional ordered states [6–8]. The case of d^4 electron filling and octahedral coordination is of particular interest, as it realizes a nominally nonmagnetic $J_{\text{eff}} = 0$, $m_{J_{\text{eff}}} = 0$ single-ion singlet [9–12], as shown in Fig. 1(a). This nonmagnetic Mott insulator state has attracted recent attention as a platform to study excitonic magnetism. Although there are no preformed local moments on $J_{\text{eff}} = 0$ ions, if the superexchange energy is comparable to the atomic spin-orbit coupling strength, then the $J_{\text{eff}} = 0$ ground state and first excited $J_{\text{eff}} = 1$ triplet can mix. Exchange driven condensation of the $J_{\text{eff}} = 1$ excited states results in an excitonic magnetic order from which novel magnetic phases can arise [13–15]. Such condensate can lead to quantum spin liquid physics when realized on a honeycomb lattice [16].

Two recently synthesized pentavalent honeycomb iridates $\text{Sr}_3\text{CaIr}_2\text{O}_9$ and NaIrO_3 display similar nearly temperature-

independent magnetic susceptibilities with small paramagnetic moments [17] that may indicate nonmagnetic $J_{\text{eff}} = 0$ Mott insulating ground states. $\text{Sr}_3\text{CaIr}_2\text{O}_9$, is a 2:1 ordered perovskite isostructural to $\text{Sr}_3\text{CaRu}_2\text{O}_9$ (space group $P21/c$) with a buckled honeycomb lattice and corner-sharing IrO_6 octahedra [18]. Structural refinements for powder x-ray and neutron diffraction indicate that there are two nonequivalent IrO_6 octahedra in the structure of $\text{Sr}_3\text{CaIr}_2\text{O}_9$, each having a different degree of cubic symmetry breaking, with a broad distribution of Ir-O bond distances. While the overall structure of the first Ir site, Ir_A , is characterized by “three-long, three-short” Ir-O bond pattern (average $\text{Ir-O}_{\text{min}}/\text{Ir-O}_{\text{max}} = 0.86$), with larger tetragonal distortions than that of $\text{Sr}_3\text{CaRu}_2\text{O}_9$ [19], the second Ir site, Ir_B , is only weakly distorted (average $\text{Ir-O}_{\text{min}}/\text{Ir-O}_{\text{max}} = 0.92$). Curie-Weiss analysis of the magnetic susceptibility finds a Weiss temperature of $\theta_{\text{CW}} = -8(5)$ K, and a small paramagnetic moment ($\mu_{\text{eff}}^{\text{Sr}} = 0.18 \mu_B/\text{Ir}$) consistent with a $J_{\text{eff}} = 0$ ground state.

However, NaIrO_3 is synthesized via oxidative Na-deintercalation of Na_2IrO_3 [20] and maintains the edge-sharing IrO_6 honeycomb lattice of the parent compound with an average $d_{\text{Ir-Ir}} \approx 3\text{\AA}$. Na-Ir stacking disorder in NaIrO_3 reduces the space group to $P\bar{1}$. Similarly to $\text{Sr}_3\text{CaIr}_2\text{O}_9$, Curie-Weiss analysis of the weakly temperature-dependent magnetic susceptibility in the temperature range $3 < T < 300$ K found small paramagnetic moment ($\mu_{\text{eff}}^{\text{Na}} = 0.18 \mu_B/\text{Ir}$) and Curie-Weiss temperature of $\theta_{\text{CW}} = 0$ K. This observation led to a description of NaIrO_3 and $\text{Sr}_3\text{CaIr}_2\text{O}_9$ as the first realizations of nonmagnetic $J_{\text{eff}} = 0$ Mott insulators on the honeycomb lattice. Thus, these materials are potential candidates to explore excitonic magnetism, but an investigation of

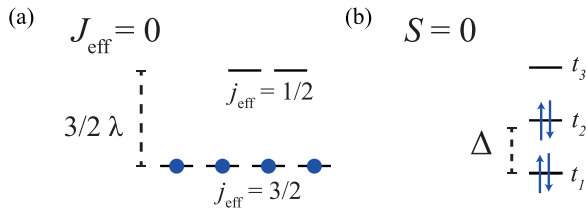


FIG. 1. Schematic of two limiting cases for an octahedrally coordinated Ir^{5+} ion: (a) $J_{\text{eff}} = 0$ state and (b) $S = 0$, with $\lambda \gg \Delta$ and $\Delta \approx \lambda \approx J_H$, respectively. t_i , $i = 1, 2, 3$ represent a linear combination of the t_{2g} orbitals for dominant Δ .

the electronic structure is first necessary to verify the $J_{\text{eff}} = 0$ nature in each compound.

The nonmagnetic $J_{\text{eff}} = 0$ ground state in octahedrally coordinated Ir^{5+} compounds is sensitive to structural details. For instance, local noncubic trigonal distortions of IrO_6 octahedra (Δ) can result in a nonzero magnetic moment. At the single-ion level, the t_{2g} orbitals for octahedrally coordinated Ir^{5+} can be described in two limiting cases of j - j coupling, $\Delta \ll \lambda$, $J_{\text{eff}} = 0$, Fig. 1(a), and Russell-Saunders coupling, $\Delta \gg \lambda$, $S = 1$. When the distortion-driven splitting of the t_{2g} orbitals is comparable to the Hund's coupling in iridates, a nonmagnetic $S = 0$ can be stabilized [21] [Fig. 1(b)]. Such a band insulating ground state with strong-spin orbit coupling is of interest in its own right because of the potential to realize flat bands and topological excitations [22]. At intermediate couplings, $\Delta/\lambda \approx 1$, noncubic crystal fields might lead to a $J_{\text{eff}} \neq 0$ ground state, as characterized by the expectation value $\langle J_{\text{eff}}^2 \rangle$ [23]. Additional departures from the single-ion limit can result from direct Ir-Ir hopping, t [24]. Interestingly, most of the investigated octahedrally coordinated pentavalent iridates fall close to the j - j coupling limit, but have been characterized by a small nonzero total angular momentum [21,23,25,26], including double perovskites Sr_2YIrO_6 [27,28], Ba_2YIrO_6 [29], and the family of $6H$ -perovskites $\text{Ba}_3\text{XIr}_2\text{O}_9$ ($\text{X} = \text{Sr}, \text{Ca}, \text{Zn}, \text{Mg}$) [24,30]. Given that the many closely competing energy scales can lead to drastically different insulating ground states with the same zero net magnetic moment, it is essential to investigate these materials using techniques that are directly sensitive to Ir $5d$ -orbital occupation and ligand environment. Such information can be obtained directly through x-ray absorption spectroscopy (XAS) and resonant inelastic x-ray scattering (RIXS) measurements at the Ir L_3 absorption edge [31–33].

In this work, we use XAS and RIXS to study the interplay of energy scales and local structural distortions in the electronic structure of the two Ir^{5+} honeycomb iridates $\text{Sr}_3\text{CaIr}_2\text{O}_9$ and NaIrO_3 . The measured RIXS spectrum in $\text{Sr}_3\text{CaIr}_2\text{O}_9$ is consistent with a nearly ideal $J_{\text{eff}} = 0$ despite the presence of tetragonally distorted IrO_6 octahedra. We find that local disorder results in a distribution of crystal field splittings that broadens the RIXS spectra for $\text{Sr}_3\text{CaIr}_2\text{O}_9$ and allows us to extract information about the distribution of energy scales from this disorder. The powder nature of our sample prevents us from resolving further broadening due to dispersion associated with spin-orbit excitonic modes [34]. However, the RIXS spectrum of NaIrO_3 is qualitatively different from that of $\text{Sr}_3\text{CaIr}_2\text{O}_9$ and all other reports for Ir^{5+} compounds. In

particular, we do not observe a well defined excitation on the scale of $3/2\lambda$. The spectra is instead comprised of a broad continuum of excitations for energy (ΔE) above 500 meV. In attempt to account for this, we first consider a single ion model for NaIrO_3 and explore the effects of different noncubic crystal fields and exchange splitting in the RIXS spectrum. Qualitative consistency between this Mott insulating scenario and the RIXS data requires large octahedral distortions and nonzero magnetic moments that interact via an Ising exchange and antiferromagnetically order above $T = 300$ K. Although not entirely ruled out by the existing data, magnetic order is unlikely in NaIrO_3 . We then consider a second model in the limit of a flat-band narrow-gap $S = 0$ insulator, in agreement with density functional theory calculations for a fully relaxed crystal structure. We find that such a band insulating state is the most likely description of the electronic state of NaIrO_3 . Our result highlights the capabilities of resonant spectroscopic x-ray techniques to provide detailed information about the local environment and electronic structure of quantum materials and further emphasizes how the many competitive energy scales in honeycomb iridates act to produce intrinsically different magnetic and electronic ground states.

II. EXPERIMENTAL DETAILS

High-quality powder samples of $\text{Sr}_3\text{CaIr}_2\text{O}_9$ and NaIrO_3 were grown as described in Ref. [17]. RIXS measurements were performed at Sector 27 (MERIX) at the advanced photon source (APS) of the Argonne National Laboratory [35]. A 2 m radius spherically diced Si(844) analyzer was used to provide an overall energy resolution (full width at half maximum, FWHM) of 33 meV. All measurements were performed with a fixed scattering angle of $2\theta = 90^\circ$ in a specular geometry. Room temperature x-ray absorption spectroscopy (XAS) was performed on $\text{Sr}_3\text{CaIr}_2\text{O}_9$, NaIrO_3 , IrO , α - Li_2IrO_3 , and $\text{Ag}_3\text{LiIr}_2\text{O}_6$, in transmission at APS 4-ID-D and analyzed using the Larch [36] software packages. Exact diagonalization and simulations of RIXS cross-sections were carried out using the EDRIXS software package [37]. The DFT calculations for NaIrO_3 were performed within the Perdew-Burke-Ernzerhof formulation of generalized gradient approximation (GGA) using the Quantum Espresso software package [38,39]. Fully relativistic potentials were used for the spin-orbit calculations. For the fully relaxed calculations, the reported lattice parameters and corresponding atomic positions, assuming perfect Na stacking [17], are allowed to vary to achieve forces in each atom below 10^{-3} Ry/a.u. and pressure below 1 kbar. A $15 \times 15 \times 15$ k-grid was used for density of states calculations.

III. EXPERIMENTAL RESULTS

A. XAS

We first examine the x-ray absorption spectra of NaIrO_3 and $\text{Sr}_3\text{CaIr}_2\text{O}_9$ to provide an overall picture of their electronic structure and to verify the Ir^{5+} oxidation state. This is a particularly important measurement for NaIrO_3 because of the possibility for mixed Ir valence. While NaIrO_3 powder phases with intermediate stoichiometry cannot be synthesized via *chimie douce* oxidative deintercalation, it is possible that the oxidation state of Ir is altered upon irradiation with an

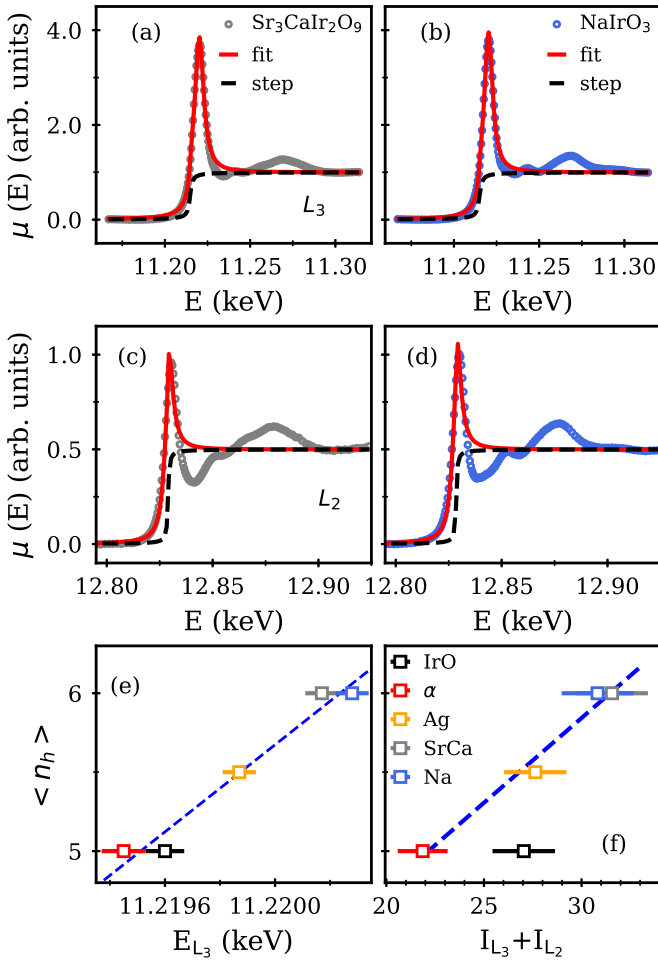


FIG. 2. (a) Ir L₃ edge XAS intensity in Sr₃CaIr₂O₉ and (b) in NaIrO₃. (c) Ir L₂ edge XAS in Sr₃CaIr₂O₉ and (d) in NaIrO₃. All data was taken at $T = 300$ K. Red line is a fit to a Lorentzian peak and an arctangent step (dotted black line), as explained in the main text. Direct comparison of the (e) L₃ white line and (f) L₃ + L₂ integrated intensity of Sr₃CaIr₂O₉ (SrCa) and NaIrO₃ (Na) to that of IrO, α -Li₂IrO₃ (α) and Ag₃LiIr₂O₆ (Ag). Dotted blue line is a linear fit.

intense x-ray beam [17]. Moreover, single crystals of Na_{0.7}IrO₃ with mixed valence Ir ($\mu_{\text{eff}} = 1.1 \mu_B/\text{Ir}$) have been recently synthesized via flux methods [40]. In Figs. 2(a) and 2(c) we show the normalized absorption intensity for Sr₃CaIr₂O₉ at the Ir L₃ and L₂ edges, respectively. The equivalent data set for NaIrO₃ is shown in Figs. 2(b) and 2(d).

To assess the Ir oxidation states, we fit the XAS white-line with a Lorentzian peak and arctangent step [41] and examine both the Ir L₃ edge peak position, E_{L_3} , [Fig. 2(e)] and the weighted sum of numerically integrated L₃ and L₂ white-line intensities [42], namely, $\langle n_h \rangle \propto I_{L_3} + (E_{L_3}/E_{L_2})I_{L_2}$ [Fig. 2(f)]. We also show the corresponding quantities determined from measurements on Ir⁴⁺ standards IrO, α -Li₂IrO₃ and an intermediate oxidation state Ag₃LiIr₂O₆ [43]. Such an analysis has successfully been used to determine the oxidation state of 5d compounds [32,43,44]. We find that the white line positions and integrated intensities are consistent with Ir⁵⁺ in both Sr₃CaIr₂O₉ and NaIrO₃. We also extract a branching ratio

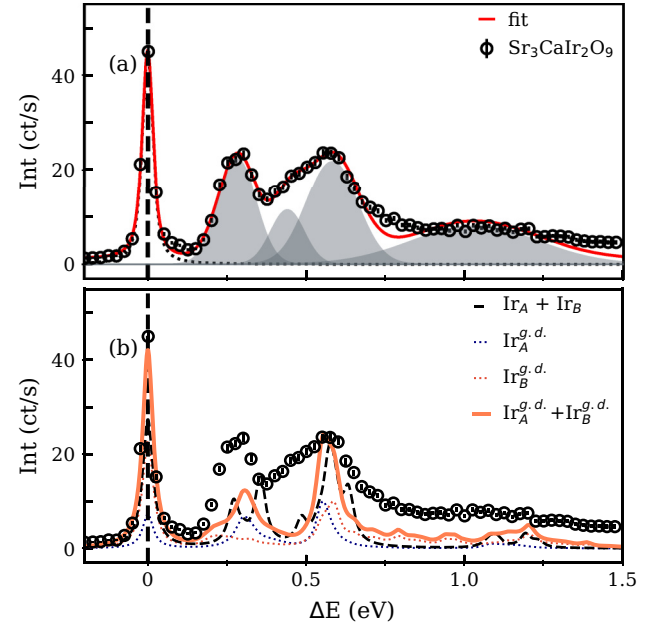


FIG. 3. (a) Ir L₃ RIXS intensity at $E_i = 11.217$ keV, in Sr₃CaIr₂O₉ at $T = 20$ K. Vertical dotted line indicates $E_{\text{loss}} = 0$. Red line is a fit to a Voigt elastic line (dotted line) and four Gaussian peaks (gray shaded). (b) Calculated powder average RIXS intensity for two Ir⁵⁺ sites with nonequivalent tetragonally distorted octahedral environments as described in the main text (black dashed line). The blue and red dotted lines show the corresponding RIXS intensities when including random tetragonal fields to account for static disorder. The total spectrum is shown in orange.

for Sr₃CaIr₂O₉ of $BR = I_{L_3}/I_{L_2} = 5.8$ and for NaIrO₃ $BR = 5.2$. These values are consistent with reports for other pentavalent iridates [32].

B. RIXS on Sr₃CaIr₂O₉

We use RIXS to reveal more detail of the electronic structure of Sr₃CaIr₂O₉. In the limit of a large cubic crystal field, weak trigonal or tetragonal distortions, and small intersite hopping, the RIXS spectrum for octahedrally coordinated Ir⁵⁺ is characterized by two low energy ($\Delta E < 1$ eV), inelastic features associated with intra- t_{2g} excitations into a $J_{\text{eff}} = 1$ triplet and a $J_{\text{eff}} = 2$ quintuplet, respectively [23] [Fig. 5(a)]. Most octahedrally coordinated Ir⁵⁺ oxides show deviations from the large cubic crystal field limit. For example, in 6H perovskites [27], the small Ir-Ir ($d_{\text{Ir-Ir}} \approx 2.75$ Å) distances promote electron delocalization and give rise to additional inelastic features in the RIXS spectrum. In Fig. 3(a), we show $T = 20$ K RIXS signal from powder samples of Sr₃CaIr₂O₉ at $E_i = 11.215$ keV for $\Delta E < 1.5$ eV. It was necessary to include four Gaussian functions with $120 < \text{FWHM} < 470$ meV and a resolution limited Voigt elastic line profile (FWHM = 33 meV) to fit the RIXS spectrum. Given the large average $d_{\text{Ir-Ir}} = 3.98(3)$ Å in Sr₃CaIr₂O₉, Ir-Ir hopping is not a likely possibility. Instead, the four RIXS features can be consistently explained to arise from inter t_{2g} transitions on two nonequivalent Ir sites and the presence of local structural disorder due to the broad distribution of Ir-O bond distances [17].

We consider a model with $U = 2$ eV, Hund's coupling = 0.285 eV, $\lambda = 0.36$ eV and two noninteracting Ir sites labeled Ir_A and Ir_B . The value of J_H and U , consistent with reported values for Ir [27,43], are chosen to provide the best description of the measured RIXS intensity. The effect of a tetragonal distortion of IrO_6 octahedra on the splitting of the Ir t_{2g} orbitals is parameterized by a crystal field Hamiltonian with nonzero diagonal terms ($\delta_1, \delta_1, \delta_2$) [37]. We allow for different magnitudes of tetragonal distortion on each site and find that the parameters $\delta_1^A = -0.18$ eV, $\delta_2^A = -0.03$ eV and $\delta_1^B = -0.1$ eV, $\delta_2^B = -0.05$ eV give reasonable agreement with the data. We include a final state lifetime of $\Gamma = 0.02$ eV [43] and powder average the calculated RIXS cross-section to compare with our data. The total intensity is shown in Fig. 3(b) (black dashed line). While this model is in qualitative agreement with our data, it does not capture the considerable broadening of the dd excitations. Attributing this broadening solely to electron delocalization would imply a minimum bandwidth of ≈ 120 meV, which is not likely given that Ir-Ir hopping is expected to be negligible in $\text{Sr}_3\text{CaIr}_2\text{O}_9$. However, local structural disorder is a possibility that cannot be ruled out with the existing powder x-ray and neutron diffraction data, since these measurements are only sensitive to the average crystalline structure. Moreover, powder neutron scattering measurements indicate that there is a broad distribution of Ir-O bond distances in $\text{Sr}_3\text{CaIr}_2\text{O}_9$ [17]. Such local structural disorder on the ligand could lead to a distribution of IrO_6 environments throughout the sample, resulting in an apparent broadening of crystal field excitations [45]. To incorporate such local disorder in RIXS spectra we consider a model that includes random tetragonal fields sampled from a normal distribution with mean values of δ_1, δ_2 and a standard deviation of $\sigma = 0.2$ eV which provide the best agreement with the data (orange line). These values are well within the ranges of non-cubic crystal fields used to model RIXS data in the literature, for example, for CaIrO_3 required a tetragonal crystal field of -750 meV [46], and trigonal fields range from 600 meV in pyrochlore iridates $\text{Y}_2\text{Ir}_2\text{O}_7$ and $\text{Eu}_2\text{Ir}_2\text{O}_7$ [47] to -75 meV in $\text{Ag}_3\text{LiIr}_2\text{O}_7$ [43]. The RIXS calculation including crystal field disorder better recovers the overall energy broadening of the data as well as the intensity ratio between inelastic features, as shown in Fig. 3. The powder nature of our samples prevents us from ruling out or confirming additional broadening due to dispersive spin-orbit excitons, as seen in other Ir^{5+} iridates [34]. This analysis highlights the utility of high resolution RIXS as a measure of local structural disorder in correlated insulators. Moreover, it allows us to directly extract an energy scale and a distribution for the local Ir-O disorder. Thus, RIXS measurements can provide complementary information to local structural measurements such as Pair Distribution Function or extended x-ray absorption fine structure [43].

Based on the mean crystal field energies from our RIXS model, we compute an average expectation value for the total angular momentum, $\langle J_{\text{eff}}^2 \rangle = 0.03$ [37]. Thus, our results confirm that $\text{Sr}_3\text{CaIr}_2\text{O}_9$ is very well described in the $j - j$ coupling limit of a $J_{\text{eff}} = 0$ Mott insulator and that the weak moment extracted from susceptibility measurements is due to magnetic impurities [17,18]. However, the large 250 meV energy gap makes magnetic exciton condensation via applica-

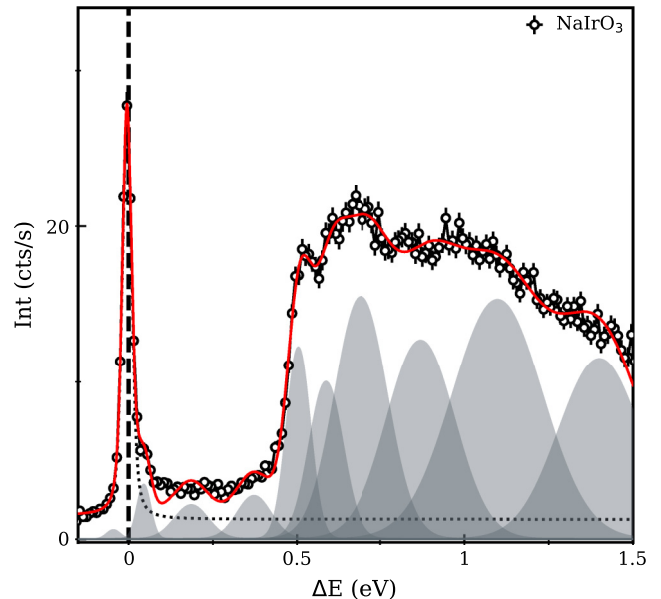


FIG. 4. Ir L_3 RIXS intensity, $E_i = 11.217$ keV, in NaIrO_3 at $T = 20$ K. Vertical dotted line indicates $E_{\text{loss}} = 0$. Red line is a fit to a Voigt elastic line (dotted line) and a set of Gaussian peaks (gray shaded).

tion of hydrostatic pressure, carrier doping or other means an unlikely possibility in this material [48–50].

C. RIXS on NaIrO_3

After having established the Ir^{5+} oxidation state, we now bring our attention to the RIXS spectrum of NaIrO_3 , shown in Fig. 4. There is a stark qualitative difference between the observed RIXS spectra for NaIrO_3 and that of $\text{Sr}_3\text{CaIr}_2\text{O}_9$. In contrast to other typical Ir^{5+} iridates that have well-defined $\Delta E \approx 250$ meV RIXS features from inter- t_{2g} split by $3/2 \lambda$ excitations [10,21,23,25,51], we observe a weak and broad inelastic signal that spans from ΔE of 0.5 eV up to 1.5 eV and can be fit to a minimum of six Gaussian peaks. Below 0.5 eV there is a nearly constant small intensity above background, but no discernible peak. In the following, we discuss possible explanations for the observed RIXS spectrum.

We start by discussing the excitation spectrum of Ir^{5+} within a single ion picture corresponding to the reported limit of a Mott insulating state in NaIrO_3 . As shown in Fig. 5(a), in an undistorted octahedral environment with $J_H = 0.285$ eV two excited states are expected for $E < 0.5$ eV, an energy scale set by the spin-orbit coupling constant, $3\lambda/2 = 0.3 - 0.5$ eV [8]. The value of J_H , consistent with reported values for Ir [27,43], is chosen to provide the best agreement between the data and the RIXS intensity calculations below. Trigonal (Δ), tetragonal (δ_1, δ_2), and other noncubic distortions (Δ_{NCF}), act to further split the t_{2g} states increasing the number of available excited states, as shown in Figs. 5(b)–5(d) for $\lambda = 0.42$ eV. We note that Δ_{NCF} parametrizes possible large noncubic crystal fields resulting from low symmetry distortions of the IrO_6 octahedra as occurs in the post-perovskite NaIrO_3 ($\mu = 0.28 \mu_B/\text{Ir}$, O-Ir-O ≈ 73.2 deg and average $d_{\text{Ir-O}} = 3.03 \text{ \AA}$). In this case, the t_{2g} crystal field Hamiltonian includes the nonzero diagonal terms

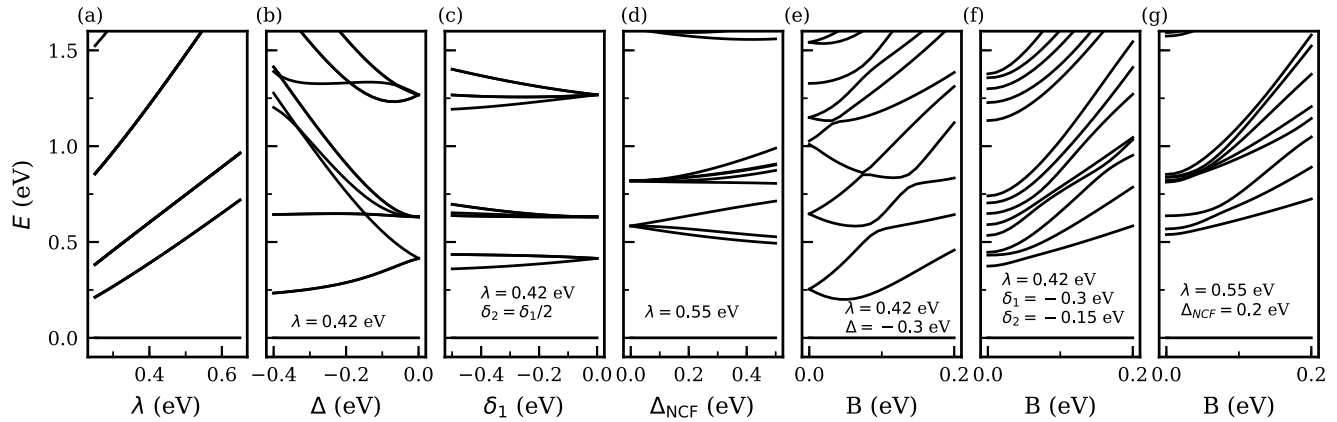


FIG. 5. Excitation spectrum for a single Ir^{5+} ions with $J_H = 0.285$ eV as a function of (a) atomic spin orbit coupling λ , (b) trigonal field, Δ , (c) tetragonal field, (δ_1, δ_2) , and (d) noncubic fields (Δ_{NCF}) . We also show the excitation spectrum as a function of exchange field for fixed values of (e) trigonal, (f) tetragonal, and (g) noncubic crystal fields.

$(\Delta_{\text{NCF}}/2, \Delta_{\text{NCF}}, 0)$ [10]. In Figs. 6(a)–6(c) we show the calculated powder averaged RIXS spectrum including a normal distribution of crystal field values to account for local ligand disorder with mean values equal to $\Delta = -0.3$ eV, $\delta_1 = -0.2$ eV with $\delta_2 = \delta_1/2.5$, and $\Delta_{\text{NCF}} = 0.2$ eV, respectively, and $\sigma = 0.1$ eV which provide the best description of the RIXS spectrum. We set $\lambda = 0.42$ eV for all the calculations except those including Δ_{NCF} for which $\lambda = 0.55$ eV. For a better

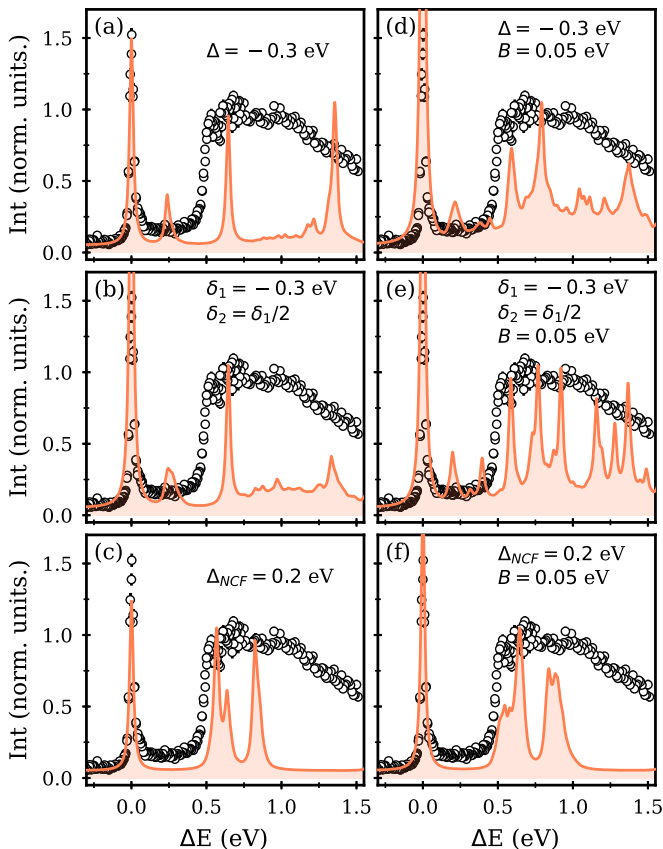


FIG. 6. Simulated single ion RIXS spectrum for different crystal field environments [(a)–(c)] and exchange splitting fields [(d)–(e)].

qualitative agreement with the data a linear background is added to the calculation. We find that these calculations fail to accurately describe the experimental data for any physically reasonable value of crystal fields.

For all three models discussed, the magnitude of the crystal field that is necessary to observe suppressed inelastic intensity in the region $E_{\text{loss}} < 0.5$ eV and obtain a broad set of excitations above $E_{\text{loss}} > 0.5$ eV leads to a $J_{\text{eff}} \neq 0$ ground state: $\langle J_{\text{eff}}^2 \Delta \rangle = 1.647$, $\langle J_{\text{eff}}^2 \delta_1, \delta_2 \rangle = 0.096$ and $\langle J_{\text{eff}}^2 \Delta_{\text{NCF}} \rangle = 0.085$. Given the finite $\langle J_{\text{eff}}^2 \rangle$ values we find, particularly for the trigonally distorted scenario, the small and weakly temperature-dependent magnetic susceptibility measured in NaIrO_3 would only be consistent with these scenarios if the nonzero magnetic moments interact with a large and dominant Ising anisotropy. The Ising interactions must result in an onset of long-range magnetic order for $T > 300$ K and thus act to freeze-out thermal magnetic fluctuations for $T < 300$ K. Magnetization measurements have not been reported above 300 K for this compound, so such a scenario is within the realm of possibility. To account for a possible magnetic order in NaIrO_3 , we include an effective in-plane exchange splitting field B in our RIXS model [37] as a way to simulate any magnetism-induced t_{2g} splitting in NaIrO_3 [52], as shown in Figs. 5(e), 5(f) and 5(g). We sample a uniform distribution with central value for $B = 0.05$ eV and $\sigma = 0.02$ eV to model local-disorder-induced modifications of magnetic interactions. The resulting spectrum shows decreased inelastic spectral weight for $\Delta E < 500$ meV and a broadening of the excitation continuum above $\Delta E > 500$ meV, as shown in Figs. 6(d) and 6(e). While these calculations produce a qualitative agreement with the data, a direct confirmation of $T < 300$ K magnetic ordering in NaIrO_3 is necessary to justify these model. We note that the effect of the exchange splitting in the case of noncubic crystal field, Fig. 6(f), is negligible as the degeneracy of the t_{2g} orbitals is already broken by the crystal field. Given the inadequacy of this model to describe the RIXS spectra above 1 eV, we believe it is not a likely scenario.

Thermodynamic and transport measurements for NaIrO_3 have so far been interpreted in terms of a $J_{\text{eff}} = 0$ Mott insulator, but the data are also generally consistent with expectations

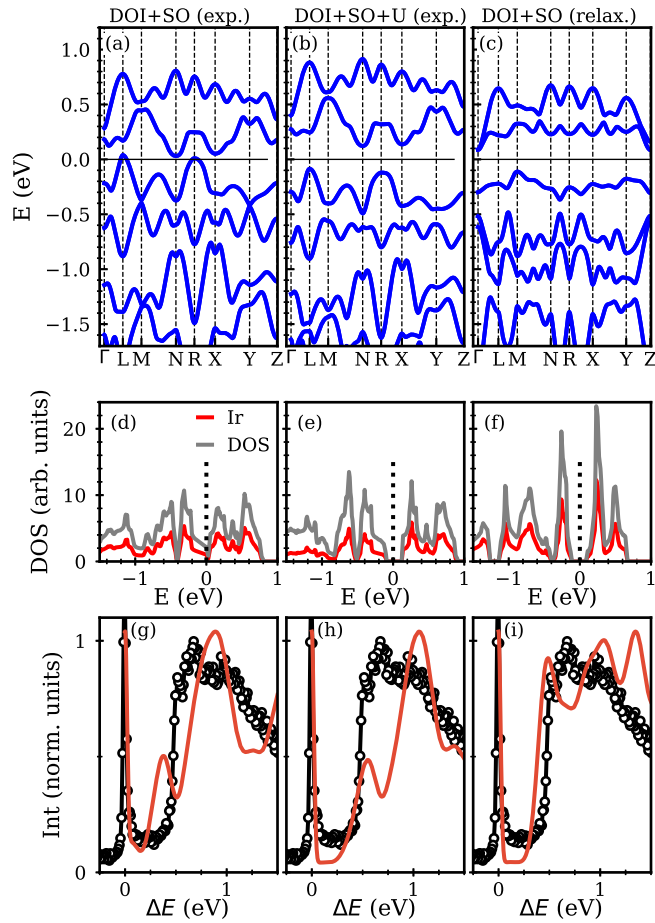


FIG. 7. (a) DFT +SO band structure and (b) DFT + SO + U band structure, with $U = 4$ eV, of NaIrO_3 for the reported structure. (c) DFT + SO band structure of NaIrO_3 for the fully relaxed structure. The associated calculated total and Ir $5d$ density of states (DOS) are shown in [(d)–(f)]. The resulting calculated RIXS spectrum compared to the measured RIXS spectrum at resonance for the reported structure is shown in panels [(g), (h)].

for a narrow gap semiconductor. Indeed, the nonmagnetic insulating post-perovskite version of NaIrO_3 ($\theta_W = -2.2$ K, $\mu_{\text{eff}} = 0.28 \mu_B/\text{Ir}$) [53] has been associated to a $S = 0$ band insulating state [Fig. 1(b)] [21,54]. To test this possibility, we have carried density functional theory calculations including spin-orbit coupling (DFT + SOI) of the band structure of NaIrO_3 as shown in Fig. 7 (see the Appendix for a non-SOI band structure calculation). These calculations were carried out using both the experimentally determined crystal structure as well as for a relaxed unit cell assuming perfect Na stacking along the c axis. The starting and relaxed lattice parameters and atomic positions are shown in the Appendix. We observe a large relaxation of the lattice and atomic positions, consistent with other reports for d^4 iridates [55] and the post-perovskite version of NaIrO_3 [21].

For both structures, our band structure calculations reveal nearly flat conduction and valence bands of mostly Ir $5d$ character [Figs. 7(a)–7(c)], as shown by our density of states calculations (DOS), shown in Figs. 7(d)–7(f). The experimental structure yields a metallic state [Fig. 7(a)], which is rendered insulating by the introduction of $U = 4$ eV, as

shown in Fig. 7(b). However, the band structure of NaIrO_3 is sensitive to the lattice parameter and atomic positions, with the fully relaxed structure yielding a band insulator with $E_{\text{gap}} = 0.5$ eV across the Brillouin Zone (BZ) [Fig. 7(c)]. This phenomenology resembles that of post-perovskite NaIrO_3 in which DFT calculations for the relaxed structure find that the largely distorted oxygen octahedra lead to a 600 meV separation of the t_{2g} states, comparable to Hund's coupling in iridates, thus stabilizing a nonmagnetic $S = 0$ state. However, for the experimental structure, the electronic structure is found to be metallic with an indirect gap and electron-electron correlations, U are necessary to obtain an insulating state [21]. Additionally, LDA + Gutzwiller calculations find that the SOI is the key player in explaining the electronic ground state of the post-perovskite NaIrO_3 , such it has been argued to be a band insulator, rather than a correlated Mott insulator [54]. We therefore consider the possibility that honeycomb NaIrO_3 is also a flat band insulator to provide an alternative explanation for the RIXS spectra. In small gap insulating materials, RIXS can be regarded as an alternative technique to electron energy loss spectroscopy to resolve the unoccupied electronic structure. Due to the localized nature of the core hole, the energy and momentum dependence of the inelastic features can be related to joint density of states of the photoexcited electron and valence hole excitations across the gap, $\text{JDOS}(Q, \Delta E)$ [56–59]. We calculate the RIXS intensity as the JDOS between an occupied and unoccupied Ir states as a function of E_{loss} [59]. Given the powder nature of our samples, the low-symmetry unit cell of NaIrO_3 and the three dimensional nature of the band structure of NaIrO_3 the calculation of a complete momentum integrated JDOS($Q, \Delta E$) over all the possible values of Q is complex and computationally expensive. We perform an approximate calculation to the JDOS involved in the RIXS process, by fixing $Q = 0$ and integrating over interband transitions along the high-symmetry directions in the Brillouin zone ($\Gamma-L-M-N-R-X-Y-Z$). The resulting RIXS intensity, convolved with the experimental resolution, is shown in Figs. 7(g)–7(i) for both $U = 0$, $U = 4$ eV, and relaxed calculations. For the experimental structure, the calculated RIXS intensity is characterized by two broad peaks with central energy depending on U . Neither calculation for $U = 0$ or $U = 4$ eV provides an agreement with the observed RIXS dispersion. However, the calculated RIXS intensity for the relaxed structure displays a continuum of excitations that sharply onsets near $E_{\text{loss}} = 500$ meV, in qualitative agreement with the NaIrO_3 RIXS spectrum. While DFT calculations tend to underestimate the gap size and a more refined calculation of the electronic structure should appropriately treat U , this analysis is strongly suggestive of NaIrO_3 being in a nonmagnetic $S = 0$ state. In this case, spin-orbit coupling generates a flat band insulating state and NaIrO_3 may be a potentially interesting platform to study topological charge excitations if a suitable means to tune the chemical potential can be found [22].

In addition to the excitations above 500 meV, we find another low energy 45 meV excitation in the RIXS spectra of NaIrO_3 that is not captured by either model. Figure 8 highlights the low-energy RIXS spectra around the elastic line. At $T = 20$ K, we observe a clear shoulder on the elastic line that can be fit with a single Gaussian centered at an energy

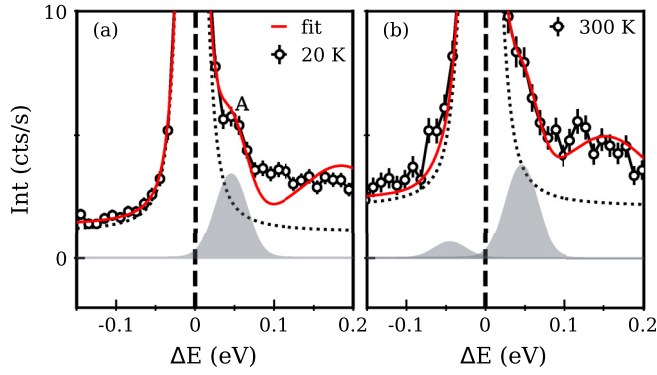


FIG. 8. Ir L_3 RIXS intensity, $E_i = 11.217$ keV, in NaIrO_3 at $T = 20$ K (a) and $T = 300$ K (b) in the range $E_{\text{loss}} = [-0.15, 0.20]$ eV. Red line is a fit to the spectrum up to 1.5 eV as described in the main text. We highlight feature A, fitted to a resolution limited Gaussian corresponding to a low energy excitation.

of 45 meV [Fig. 8(a)]. This feature is also apparent in the thermally broadened elastic line at 300 K and its intrinsic origin is confirmed by the appearance of the corresponding excitation on the energy gain side, with an intensity following detailed balance [Fig. 8(b)]. No charge excitations at 45 meV are predicted in either the large spin-orbit coupling $J_{\text{eff}}=0$ model, or the band insulating $S=0$ model. We associate this feature to scattering from phonons which, although expected to be minimal in our 90 degree scattering angle configuration, cannot be ruled out [60,61]. It is worth noticing that in the less likely scenario of a $J_{\text{eff}}=0$ magnetic ground state in NaIrO_3 , the Ir moments must then be magnetically ordered and interact through a dominant Ising anisotropy to be consistent with the observed magnetic susceptibility. A lower bound on the magnetic interaction strength, J for a mean field Ising magnetic on the honeycomb lattice may be estimated by setting the Curie Temperature T_c to the upper temperature limit of susceptibility measurements, giving an upper limit $J > 2/3k_B \times 300 \approx 16$ meV. In this scenario, weakly dispersing and gaped spin-waves would appear on an energy scale of at least $3J \approx 48$ meV, for $S = 1$.

IV. CONCLUSIONS

In summary, we have harnessed the unique capability of RIXS to probe the local electronic structure of insulating compounds to identified two different electronic ground states

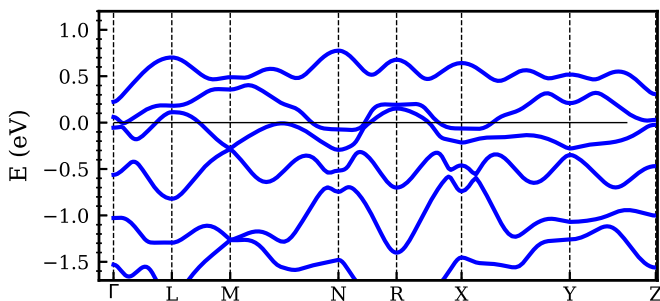


FIG. 9. Calculated band structure of NaIrO_3 without SOI.

TABLE I. Summary of the experimental and reduced atomic positions for the experimentally reported structure and the fully relaxed cell.

Atom	Exp. Cell			Reduced Cell		
	x	y	z	x	y	z
Ir	0.164	0.156	0.010	0.170	0.162	0.001
Na	0.500	0.500	0.000	0.500	0.500	0.000
Na	0.500	0.500	0.500	0.500	0.500	0.000
O	0.948	0.468	0.153	0.987	0.493	0.189
O	0.239	0.844	0.206	0.236	0.870	0.182
O	0.639	0.103	0.190	0.613	0.117	0.182

in two newly synthesized Ir^{5+} honeycomb iridates. Although, the powder nature of our samples obscures any spin-orbit exciton related dispersion [34] our RIXS measurements on $\text{Sr}_3\text{CaIr}_2\text{O}_9$ are consistent with the proposed $J_{\text{eff}}=0$ singlet. This constitutes the first realization of a nonmagnetic honeycomb iridate. $\text{Sr}_3\text{CaIr}_2\text{O}_9$ contrasts with other Ir^{5+} iridates, for example, Sr_2YIrO_6 [27,28], where substantial hopping between Ir sites leads to the formation of magnetically ordered states. However, the RIXS spectra of NaIrO_3 departs from that of other pentavalent iridates and cannot be explained within the single ion excitation spectrum. Based on DFT + SOI calculations, we propose that the largely distorted local Ir environment leads to a band insulator $S=0$ ground state. We hope our results lead to future higher temperature magnetic susceptibility or low temperature isothermal magnetization measurements required to confirm Ising magnetism. It is also highly desirable to further sample growth efforts to obtain single crystals so that the momentum dependence of the electron-hole excitations can be measured and rule out a possible Ising-like magnetic transition in NaIrO_3 . Our results highlight the potential of RIXS to distinguish a Mott insulator from a band insulator in nonmagnetic insulating materials where thermodynamic measurements cannot provide such a distinction.

ACKNOWLEDGMENTS

We acknowledge helpful conversations with M. DiScala, J. H. Kim, and M. Dean. Work at Brown University was supported by the U.S. Department of Energy, Office of Science, Office of Basic Energy Sciences, under Award No. DE-SC002165. T.M.M. and J.C. acknowledge support from the Institute for Quantum Matter, an Energy Frontier Research Center funded by the U.S. Department of Energy, Office of Science, Office of Basic Energy Sciences, under Award No. DE-SC0019331. Use of the Advanced Photon Source at Argonne National Laboratory was supported by the U.S. Department of Energy, Office of Science, Office of Basic Energy Sciences, under Contract No. DE-AC02-06CH11357.

APPENDIX

In Fig. 9 we show the calculated band structure of NaIrO_3 without SOI. The resulting dispersion is metallic, highlighting

the role of spin-orbit coupling in driving the band insulating state in NaIrO₃.

In Table I we show the atomic positions for the experimental [$a = 5.281$ (Å), $b = 5.287$ (Å), $c = 6.00$ (Å), $\alpha = 90.002^\circ$,

$\beta = 115.7^\circ$, $\gamma = 60.11^\circ$] and relaxed unit cell [$a = 5.509$ (Å), $b = 5.399$ (Å), $c = 6.708$ (Å), $\alpha = 104.1^\circ$, $\beta = 121.27^\circ$, $\gamma = 59.39^\circ$].

-
- [1] B. J. Kim, H. Jin, S. J. Moon, J.-Y. Kim, B.-G. Park, C. S. Leem, J. Yu, T. W. Noh, C. Kim, S.-J. Oh, J.-H. Park, V. Durairaj, G. Cao, and E. Rotenberg, *Phys. Rev. Lett.* **101**, 076402 (2008).
- [2] G. Jackeli and G. Khaliullin, *Phys. Rev. Lett.* **102**, 017205 (2009).
- [3] G. Chen, R. Pereira, and L. Balents, *Phys. Rev. B* **82**, 174440 (2010).
- [4] M. G. Yamada, M. Oshikawa, and G. Jackeli, *Phys. Rev. Lett.* **121**, 097201 (2018).
- [5] W. M. H. Natori, E. C. Andrade, and R. G. Pereira, *Phys. Rev. B* **98**, 195113 (2018).
- [6] A. S. Erickson, S. Misra, G. J. Miller, R. R. Gupta, Z. Schlesinger, W. A. Harrison, J. M. Kim, and I. R. Fisher, *Phys. Rev. Lett.* **99**, 016404 (2007).
- [7] W. Witczak-Krempa, G. Chen, Y. B. Kim, and L. Balents, *Annu. Rev. Condens. Matter Phys.* **5**, 57 (2014).
- [8] J. G. Rau, E. K.-H. Lee, and H.-Y. Kee, *Annu. Rev. Condens. Matter Phys.* **7**, 195 (2016).
- [9] G. Cao and P. Schlottmann, *Rep. Prog. Phys.* **81**, 042502 (2018).
- [10] S. Bhowal and I. Dasgupta, *J. Phys.: Condens. Matter* **33**, 453001 (2021).
- [11] K. Pajskr, P. Novák, V. Pokorný, J. Kolorenč, R. Arita, and J. Kuneš, *Phys. Rev. B* **93**, 035129 (2016).
- [12] Y. Zhang, L.-F. Lin, A. Moreo, and E. Dagotto (2022), [arXiv:2206.05223](https://arxiv.org/abs/2206.05223)
- [13] G. Khaliullin, *Phys. Rev. Lett.* **111**, 197201 (2013).
- [14] C. Svoboda, M. Randeria, and N. Trivedi, *Phys. Rev. B* **95**, 014409 (2017).
- [15] O. N. Meetei, W. S. Cole, M. Randeria, and N. Trivedi, *Phys. Rev. B* **91**, 054412 (2015).
- [16] C. Xu, J. Feng, M. Kawamura, Y. Yamaji, Y. Nahas, S. Prokhorenko, Y. Qi, H. Xiang, and L. Bellaïche, *Phys. Rev. Lett.* **124**, 087205 (2020).
- [17] D. C. Wallace and T. M. McQueen, *Dalton Trans.* **44**, 20344 (2015).
- [18] X. Chen and S. D. Wilson, *Phys. Rev. B* **94**, 195115 (2016).
- [19] J. T. Rijssenbeek, S. Malo, V. Caignaert, and K. R. Poeppelmeier, *J. Am. Chem. Soc.* **124**, 2090 (2002).
- [20] Y. Singh and P. Gegenwart, *Phys. Rev. B* **82**, 064412 (2010).
- [21] S. Bhowal, S. Baidya, I. Dasgupta, and T. Saha-Dasgupta, *Phys. Rev. B* **92**, 121113(R) (2015).
- [22] W. Zhang, Z. Addison, and N. Trivedi, *Phys. Rev. B* **104**, 235202 (2021).
- [23] S. Bhowal and I. Dasgupta, *J. Magn. Magn. Mater.* **507**, 166827 (2020).
- [24] A. Nag, S. Bhowal, M. M. Sala, A. Efimenko, I. Dasgupta, and S. Ray, *Phys. Rev. Lett.* **123**, 017201 (2019).
- [25] S. Bhowal and I. Dasgupta, *Phys. Rev. B* **97**, 024406 (2018).
- [26] A. A. Aczel, Q. Chen, J. P. Clancy, C. dela Cruz, D. R. Plessis, G. J. MacDougall, C. J. Pollock, M. H. Upton, T. J. Williams, N. LaManna, J. P. Carlo, J. Beare, G. M. Luke, and H. D. Zhou (2022), [arXiv:2204.05384](https://arxiv.org/abs/2204.05384).
- [27] B. Yuan, J. P. Clancy, A. M. Cook, C. M. Thompson, J. Greedan, G. Cao, B. C. Jeon, T. W. Noh, M. H. Upton, D. Casa, T. Gog, A. Paramekanti, and Y.-J. Kim, *Phys. Rev. B* **95**, 235114 (2017).
- [28] G. Cao, T. F. Qi, L. Li, J. Terzic, S. J. Yuan, L. E. DeLong, G. Murthy, and R. K. Kaul, *Phys. Rev. Lett.* **112**, 056402 (2014).
- [29] A. Nag, S. Bhowal, A. Chakraborty, M. M. Sala, A. Efimenko, F. Bert, P. K. Biswas, A. D. Hillier, M. Itoh, S. D. Kaushik, V. Siruguri, C. Meneghini, I. Dasgupta, and S. Ray, *Phys. Rev. B* **98**, 014431 (2018).
- [30] A. Nag, S. Middey, S. Bhowal, S. K. Panda, R. Mathieu, J. C. Orain, F. Bert, P. Mendels, P. G. Freeman, M. Mansson, H. M. Ronnow, M. Telling, P. K. Biswas, D. Sheptyakov, S. D. Kaushik, V. Siruguri, C. Meneghini, D. D. Sarma, I. Dasgupta, and S. Ray, *Phys. Rev. Lett.* **116**, 097205 (2016).
- [31] L. J. P. Ament, G. Khaliullin, and J. van den Brink, *Phys. Rev. B* **84**, 020403(R) (2011).
- [32] J. P. Clancy, N. Chen, C. Y. Kim, W. F. Chen, K. W. Plumb, B. C. Jeon, T. W. Noh, and Y.-J. Kim, *Phys. Rev. B* **86**, 195131 (2012).
- [33] H. Gretarsson, J. P. Clancy, X. Liu, J. P. Hill, E. Bozin, Y. Singh, S. Manni, P. Gegenwart, J. Kim, A. H. Said, D. Casa, T. Gog, M. H. Upton, H.-S. Kim, J. Yu, V. M. Katukuri, L. Hozoi, J. van den Brink, and Y.-J. Kim, *Phys. Rev. Lett.* **110**, 076402 (2013).
- [34] Z. Porter, P. M. Sarte, T. Petersen, M. H. Upton, L. Hozoi, and S. D. Wilson (2022), [arXiv:2206.04721](https://arxiv.org/abs/2206.04721).
- [35] Yu. V. Shvyd'ko, J. Hill, C. Burns, D. Coburn, B. Brajuskovic, D. Casa, K. Goetze, T. Gog, R. Khachatryan, J.-H. Kim, C. Kodituwakku, M. Ramanathan, T. Roberts, A. Said, H. Sinn, D. Shu, S. Stoupin, M. Upton, M. Wiczorek, and H. Yavas, *J. Electron Spectrosc. Relat. Phenom.* **188**, 140 (2013).
- [36] M. Newville, *J. Phys.: Conf. Ser.* **430**, 012007 (2013).
- [37] Y. Wang, G. Fabbri, M. Dean, and G. Kotliar, *Comput. Phys. Commun.* **243**, 151 (2019).
- [38] P. Giannozzi, S. Baroni, N. Bonini, M. Calandra, R. Car, C. Cavazzoni, D. Ceresoli, G. L. Chiarotti, M. Cococcioni, I. Dabo, A. D. Corso, S. de Gironcoli, S. Fabris, G. Fratesi, R. Gebauer, U. Gerstmann, C. Gougoussis, A. Kokalj, M. Lazzeri, L. Martin-Samos *et al.*, and *J. Phys.: Condens. Matter* **21**, 395502 (2009).
- [39] P. Giannozzi Jr., O. Andreussi, T. Brumme, O. Bunau, M. B. Nardelli, M. Calandra, R. Car, C. Cavazzoni, D. Ceresoli, M. Cococcioni, N. Colonna, I. Carnimeo, A. D. Corso, S. de Gironcoli, P. Delugas, R. A. DiStasio, A. Ferretti, A. Floris, G. Fratesi, G. Fugallo *et al.*, *J. Phys.: Condens. Matter* **29**, 465901 (2017).
- [40] H. Zhao, B. Hu, F. Ye, M. Lee, P. Schlottmann, and G. Cao, *Phys. Rev. B* **104**, L041108 (2021).
- [41] C. Donnerer, M. M. Sala, S. Pascarelli, A. D. Rosa, S. N. Andreev, V. V. Mazurenko, T. Irifune, E. C. Hunter, R. S.

- Perry, and D. F. McMorrow, *Phys. Rev. B* **97**, 035106 (2018).
- [42] B. Qi, I. Perez, P. H. Ansari, F. Lu, and M. Croft, *Phys. Rev. B* **36**, 2972 (1987).
- [43] A. de la Torre, B. Zager, F. Bahrami, M. DiScala, J. R. Chamorro, M. H. Upton, G. Fabbris, D. Haskel, D. Casa, T. M. McQueen, F. Tafti, and K. W. Plumb, *Phys. Rev. B* **104**, L100416 (2021).
- [44] M. A. Laguna-Marco, P. Kayser, J. A. Alonso, M. J. Martínez-Lope, M. van Veenendaal, Y. Choi, and D. Haskel, *Phys. Rev. B* **91**, 214433 (2015).
- [45] C. Mauws, N. Hiebert, M. L. Rutherford, H. D. Zhou, Q. Huang, M. B. Stone, N. P. Butch, Y. Su, E. S. Choi, Z. Yamani, and C. R. Wiebe, *J. Phys.: Condens. Matter* **33**, 245802 (2021).
- [46] M. Moretti Sala, S. Boseggia, D. F. McMorrow, and G. Monaco, *Phys. Rev. Lett.* **112**, 026403 (2014).
- [47] L. Hozoi, H. Gretarsson, J. P. Clancy, B.-G. Jeon, B. Lee, K. H. Kim, V. Yushankhai, P. Fulde, D. Casa, T. Gog, J. Kim, A. H. Said, M. H. Upton, Y.-J. Kim, and J. van den Brink, *Phys. Rev. B* **89**, 115111 (2014).
- [48] T. Feldmaier, P. Strobel, M. Schmid, P. Hansmann, and M. Daghofer, *Phys. Rev. Res.* **2**, 033201 (2020).
- [49] J. c. v. Chaloupka and G. Khaliullin, *Phys. Rev. Lett.* **116**, 017203 (2016).
- [50] T. Takayama, M. Blankenhorn, J. Bertinshaw, D. Haskel, N. A. Bogdanov, K. Kitagawa, A. N. Yaresko, A. Krajewska, S. Bette, G. McNally, A. S. Gibbs, Y. Matsumoto, D. P. Sari, I. Watanabe, G. Fabbris, W. Bi, T. I. Larkin, K. S. Rabinovich, A. V. Boris, H. Ishii *et al.* (2022), [arXiv:2205.12123](https://arxiv.org/abs/2205.12123).
- [51] B. A. Duell, J. Li, D. Haskel, J. Kim, H. Park, P. G. LaBarre, A. P. Ramirez, and M. A. Subramanian, *Phys. Rev. Mater.* **5**, 054604 (2021).
- [52] H. Fujiwara, R. Y. Umetsu, F. Kuroda, J. Miyawaki, T. Kashiuchi, K. Nishimoto, K. Nagai, A. Sekiyama, A. Irizawa, Y. Takeda, Y. Saitoh, T. Oguchi, Y. Harada, and S. Suga, *Sci. Rep.* **11**, 18654 (2021).
- [53] M. Bremholm, S. Dutton, P. Stephens, and R. Cava, *J. Solid State Chem.* **184**, 601 (2011).
- [54] L. Du, X. Sheng, H. Weng, and X. Dai, *Europhys. Lett.* **101**, 27003 (2013).
- [55] Y. Li and R. Valentí, *Phys. Rev. B* **105**, 115123 (2022).
- [56] Y. Ma, N. Wassdahl, P. Skytt, J. Guo, J. Nordgren, P. D. Johnson, J.-E. Rubensson, T. Boske, W. Eberhardt, and S. D. Kevan, *Phys. Rev. Lett.* **69**, 2598 (1992).
- [57] S. Shin, A. Agui, M. Watanabe, M. Fujisawa, Y. Tezuka, and T. Ishii, *Phys. Rev. B* **53**, 15660 (1996).
- [58] V. N. Strocov, T. Schmitt, J.-E. Rubensson, P. Blaha, T. Paskova, and P. O. Nilsson, *Phys. Rev. B* **72**, 085221 (2005).
- [59] C. Monney, K. J. Zhou, H. Cercellier, Z. Vydrova, M. G. Garnier, G. Monney, V. N. Strocov, H. Berger, H. Beck, T. Schmitt, and P. Aebi, *Phys. Rev. Lett.* **109**, 047401 (2012).
- [60] S. Moser, S. Fatale, P. Krüger, H. Berger, P. Bugnon, A. Magrez, H. Niwa, J. Miyawaki, Y. Harada, and M. Grioni, *Phys. Rev. Lett.* **115**, 096404 (2015).
- [61] S. Fatale, S. Moser, J. Miyawaki, Y. Harada, and M. Grioni, *Phys. Rev. B* **94**, 195131 (2016).